Electronic Supplementary Material (ESI) for Inorganic Chemistry Frontiers.

Electronic Supplementary Material

A Nickel–Salen as a Model for Bifunctional OER/UOR Electrocatalysts: Pyrolysis Temperature–Electrochemical Activity Interconnection

Li Li[a], Lu Wang[a], Xu Peng[a,*], Shi Tao[b*]and Ming-Hua Zeng[a,c *]

[a] *Hubei Collaborative Innovation Center for Advanced Organic Chemical Materials, Ministry-of-Education Key Laboratory for the Synthesis and Application of Organic Functional Molecules & College of Chemistry & Chemical Engineering, Hubei University, Wuhan, 430062, P. R. China.*

[b] *School of Electronic and Information Engineering, Jiangsu Laboratory of Advanced Functional Materials, Changshu Institute of Technology, Changshu 215500, P. R. China.*

[c] *School of Chemistry and Pharmaceutical Sciences, Guangxi Normal University, Key Laboratory for the Chemistry and Molecular Engineering of Medicinal Resources, Guilin, 541004, P. R. China.*

Contents

Figure S11	TG profile of 3-MeOsalophen-ligand (Bis[3-Methoxysalicylydene]-1,2 Iminophenylenediamine).
Figure S12	MS curve of 3-MeOsalophen-ligand on pyrolysis.
Figure S13	Cyclic voltammetry curves of S-Ni-T at different sweeping speeds in 1.0 M KOH aqueous solution.
Figure S14	Cyclic voltammetry curves of S-Ni-T at different sweeping speeds at 1 M KOH+0.33M Urea solution.
Figure S15	C_{dl} values of S-NI-T(700, 800, 900) catalysts according to CV curve fitting.
Figure S16	Powder XRD patterns of S-Ni-800 before and after.
Figure S17	HRTEM image of S-Ni-800 after UOR.
Figure S18	High resolution XPS spectrum of S-Ni-800 after OER.
Figure S19	High resolution XPS spectrum of S-Ni-800 after long lime UOR.

Table S1 Crystallographic data for S-Ni.

Compounds	**S-Ni**
Formula	$C_{26}H_{28}NiN_3O_4$
Formula weight	505.22
T (K)	293
Crystal system	monoclinic
Space group	$P2_1/c$
a (Å)	13.4241(3)
b (Å)	14.0617(2)
c (Å)	13.1673(3)
α (°)	90
β (°)	107.797(2)
γ (°)	90
V (Å^3)	2366.59(9)
Z	4
D_c.(g cm^{-3})	1.418
μ (mm^{-1})	1.496
Reflns coll.	12376
Unique reflns	4228
R_{int}	0.0163
$R_1{}^a$[I ≥ 2σ(I)]	0.0350
$wR_2{}^b$ (all data)	0.1084
GOF	1.060

$^aR_1=\sum||F_o| - |F_c||/\sum|F_o|$. $^bwR_2=[\sum w(F_o^2 - F_c^2)^2/\sum w(F_o^2)^2]^{1/2}$.

Table S2 Selected Bond lengths (Å) and angles (°) for S-Ni.

Ni1-O3	**1.8414(12)**	**Ni1-O2**	**1.8420(12)**	**Ni1-N2**	**1.8522(13)**
O3-Ni1-N2	**95.16(6)**	**O3-Ni1-N1**	**178.80(6)**	**O2-Ni1-O3**	**83.64(5)**
O2-Ni1-N1	**95.18(6)**	**N2-Ni1-N1**	**86.02(6)**	**Ni1-N1**	**1.8562(14)**
O2-Ni1-N2	**178.59(6)**				

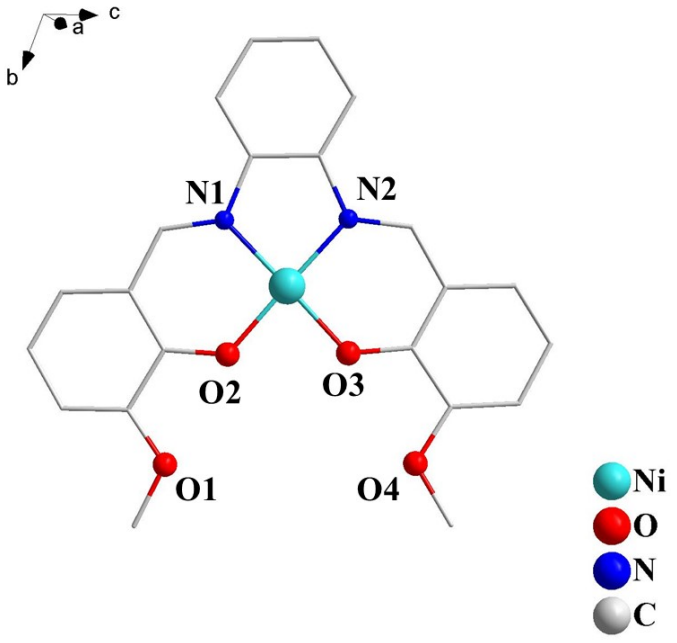

Figure S1 View of the S-Ni Complex showing the intramolecular.

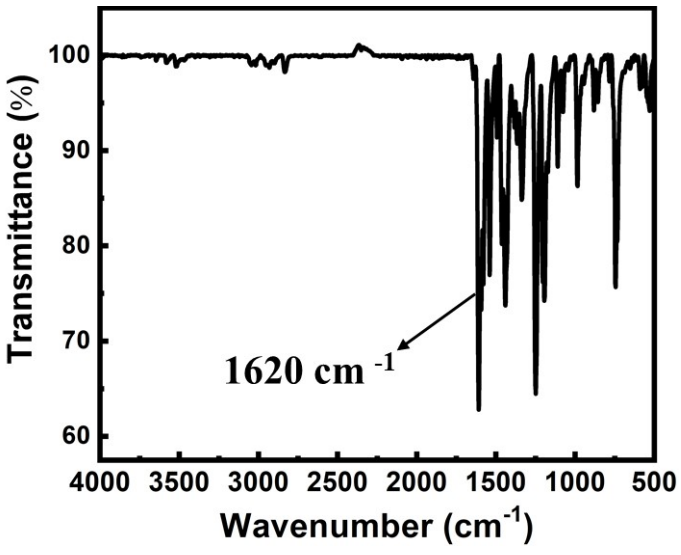

Figure S2 The IR spectrum for S-Ni.

Table S3 Element Ni content at different pyrolysis temperatures of S-Ni.

Pyrolysis Temperature	**Ni (wt %)**
700 °C	61.2
800 °C	67.9
900 °C	66.1

Table S4 Phase information and phase changes for S-Ni-T (700, 800,900).

Phases / **Samples**	**NiO** JCPDS 47-1049	**Ni** JCPDS 04-0840
S-Ni-700	(111) (200) (220)	(111) (200) (220)
S-Ni-800	(200) (220)	(111) (200) (220)
S-Ni-900	(111) (200) (220)	(111) (200) (220)

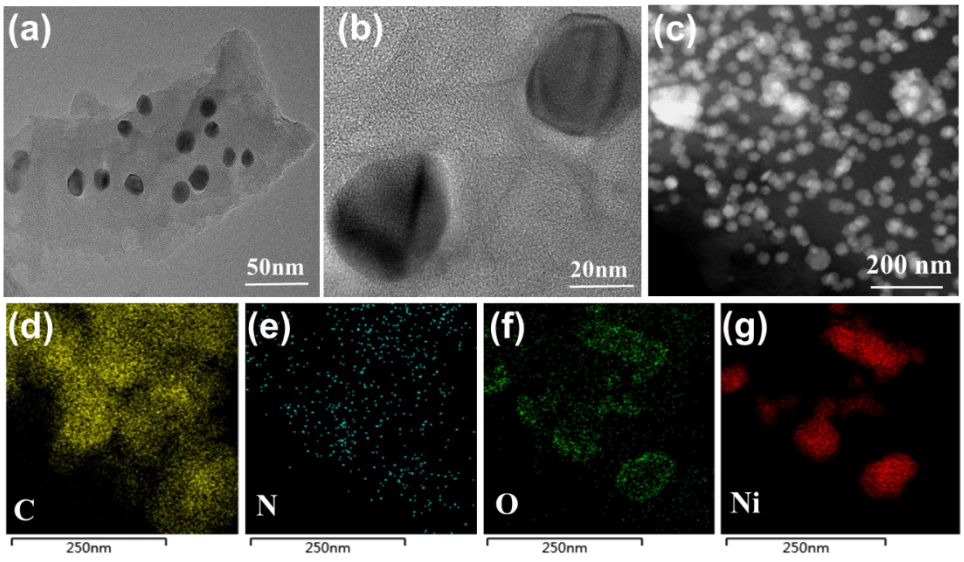

Figure S3 HRTEM image of S-Ni-T synthesized by S-Ni at pyrolysis temperature of (a) 700°C, (b) 900 °C. (c) HAADF image of S-Ni-800. (d-g) Elemental mapping images of S-Ni-800.

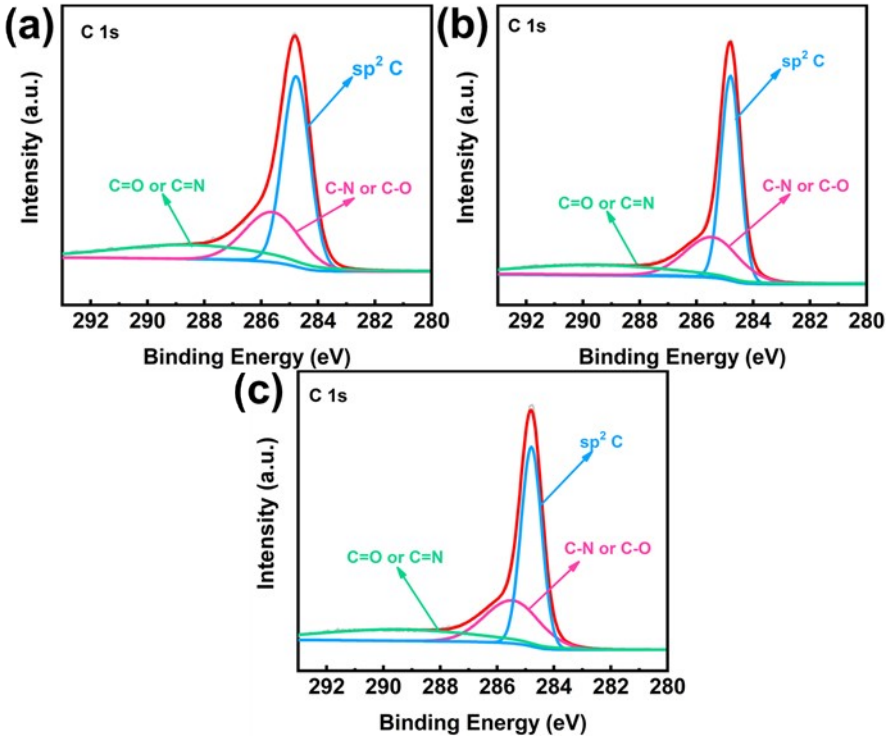

Figure S4 High resolution XPS spectrum of C 1s Peak of S-Ni-T synthesized by S-Ni at (a) 700 °C, (b) 800 °C. (c) 900 °C.

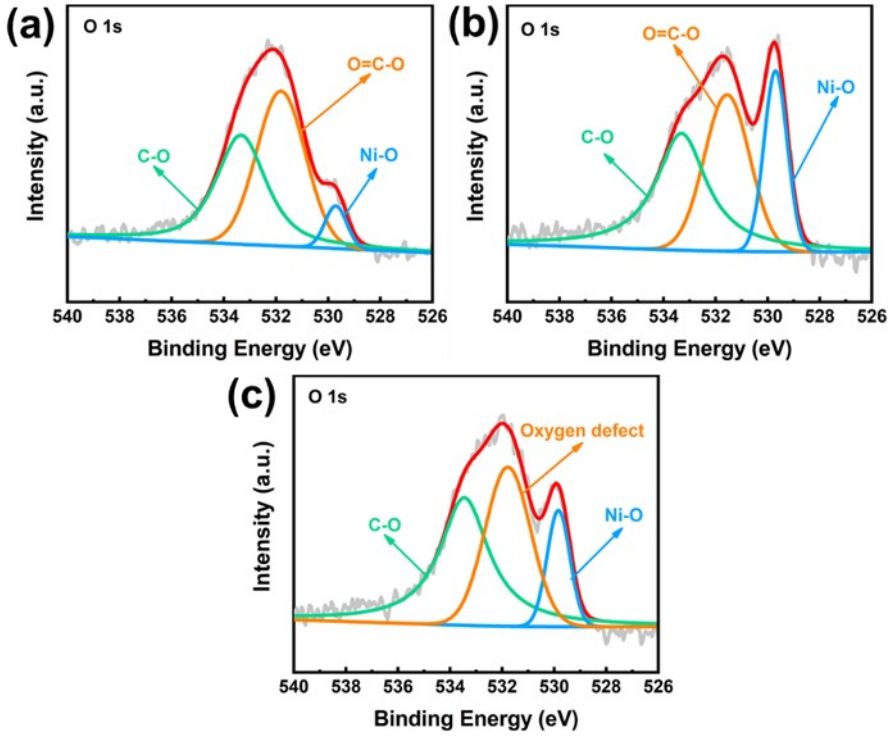

Figure S5 High resolution XPS spectrum of O 1s Peak of S-Ni-T synthesized by S-Ni at (a) 700 °C, (b) 800 °C, (b) 900 °C.

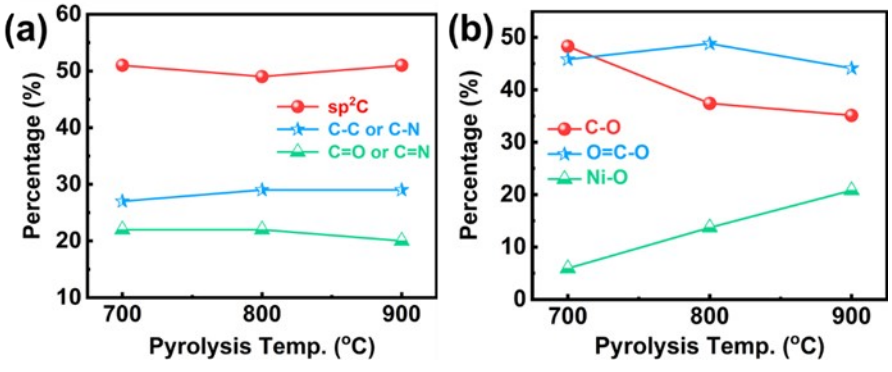

Figure S6 Composition of S-Ni-T as a function of pyrolysis temperatures: percentages of the difference: (a) C and (b) O species presented in S-Ni-T.

Table S5 Fitting results for C 1s spectra of S-Ni with different pyrolysis temperatures.

Species / Samples	sp^2C (%)	C-N or C-O (%)	C=N or C=O (%)
	284.8 eV	**285.4-285.6 eV**	**288.3-288.7 eV**
700 °C	50.9	26.7	22.4
800 °C	49.5	28.5	22.0
900 °C	51.1	28.8	20.1

Table S6 Fitting results for O 1s spectra of S-Ni with different pyrolysis temperatures.

Species / Samples	Ni-O (%)	O-C=O (%)	C-O (%)
	530.0 eV	**531.8 eV**	**533.5 eV**
700 °C	5.9	48.3	45.8
800 °C	13.8	37.4	48.8
900 °C	20.8	35.1	44.1

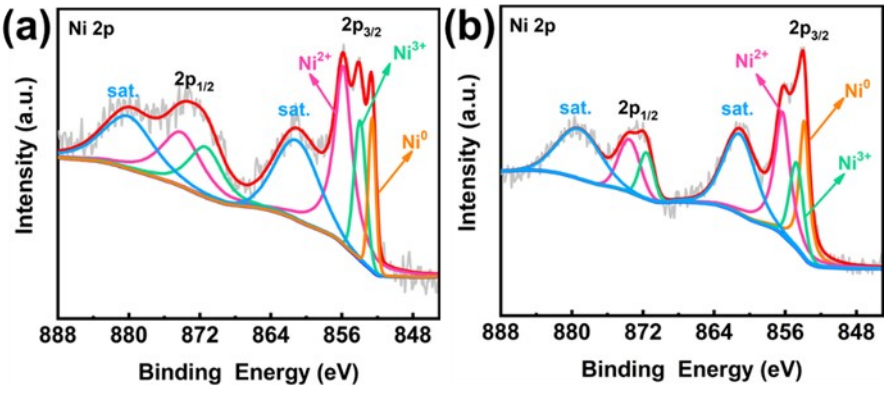

Figure S7 High resolution XPS spectra of Ni 2p peaks of S-Ni-T synthesized by S-Ni (a) 700 °C, (b) 900 °C.

Table S7 Fitting results of Ni 2p spectra of S-Ni with different pyrolysis temperatures.

Species / Samples	Ni (%)	Ni^{2+} (%)	Ni^{3+} (%)
	852.6-853.0 eV	**855.7-856.2 eV**	**853.7-854.3 eV**
700 °C	15.5	62.4	22.1
800 °C	8.4	61.2	30.4
900 °C	28.7	48.5	22.8

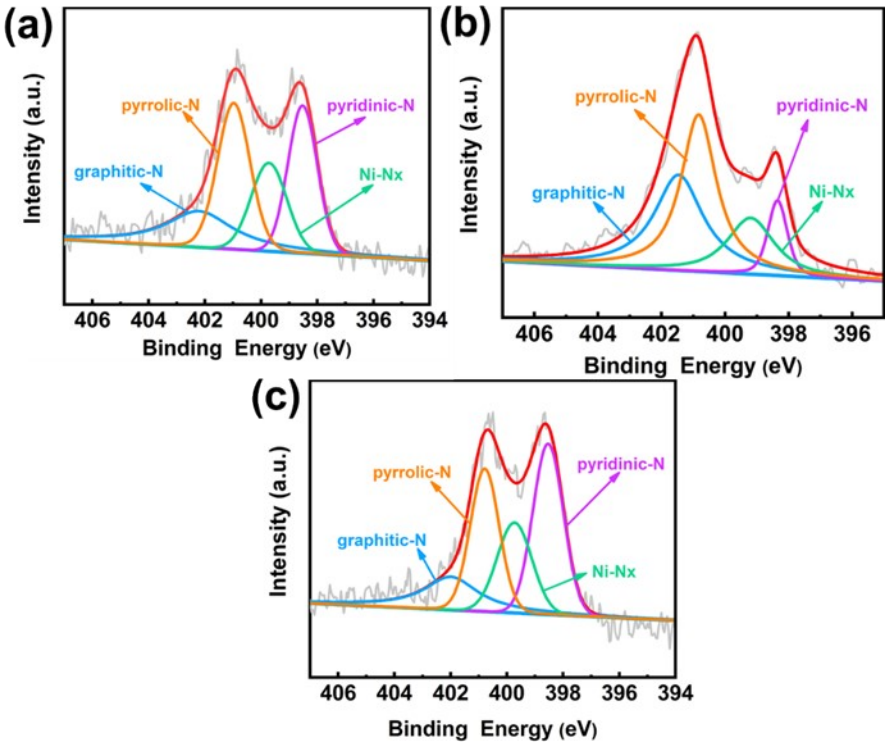

Figure S8 High resolution XPS spectrum of N 1s peak of S-Ni-T synthesized by S-Ni at (a) 700 °C, (b) 800 °C, (c) 900 °C.

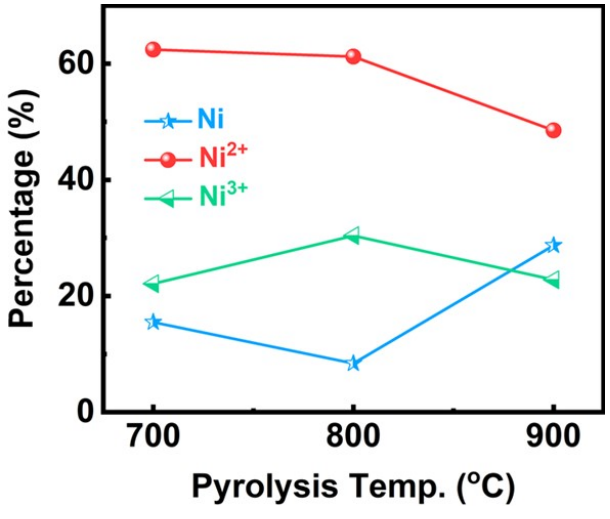

Figure S9 Composition of S-Ni-T as a function of pyrolysis temperatures: percentages of the difference: Ni species presented in S-Ni-T.

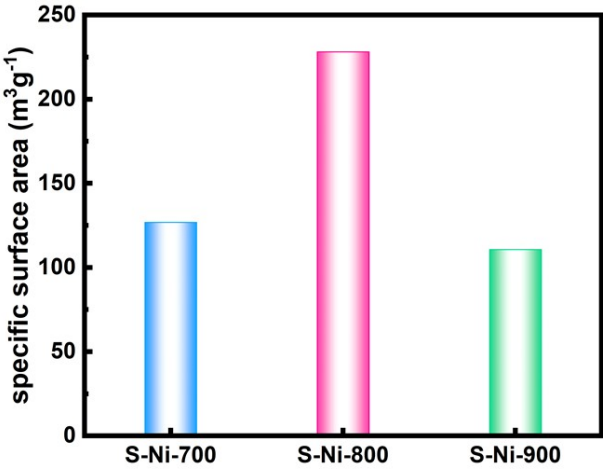

Figure S10 BET results at 77K from N_2 adsorption isothermals for all samples.

Table S8 Fitting results for N 1s spectra of S-Ni with different pyrolysis temperatures.

Species / Samples	Graphitic-N (%)	Ni-N_x (%)	Pyridine-N (%)	Pyrrolic-N (%)
	402.2 eV	**399.7 eV**	**398.8 eV**	**400.9 eV**
700 °C	22.7	19.6	26.9	30.8
800 °C	33.0	17.1	19.7	31.2
900 °C	34.1	17.8	8.5	39.7

Table S9 EXAFS fitting parameters at the Ni K-edge for various samples.

Sample	Shell	*CN*	*R*(Å)	σ^2(Å^2)	R_f(%)
Ni foil	Ni-Ni	12	2.48	0.006	0. 3
Ni-compound	Ni-N/O	5.73	1.859	0.002	0.7
	Ni-Ni	8.5	2.48	0.002	
S-Ni-700	Ni-N/O	0.74	2.00	0.010	1.1
	Ni-Ni	9.26	2.48	0.006	
S-Ni-800	Ni-N/O	0.90	2.06	0.004	1.2
	Ni-Ni	9.87	2.48	0.006	
S-Ni-900	Ni-N/O	0.81	2.07	0.0045	1.0
	Ni-Ni	9.92	2.48	0.0055	

CN: coordination numbers; *R*: bond distance; σ^2: Debye-Waller factors; *R* factor: goodness of fit. *S*02 was set to 0.815, according to the experimental EXAFS fit of Ni foil reference by fixing CN as the known crystallographic value.

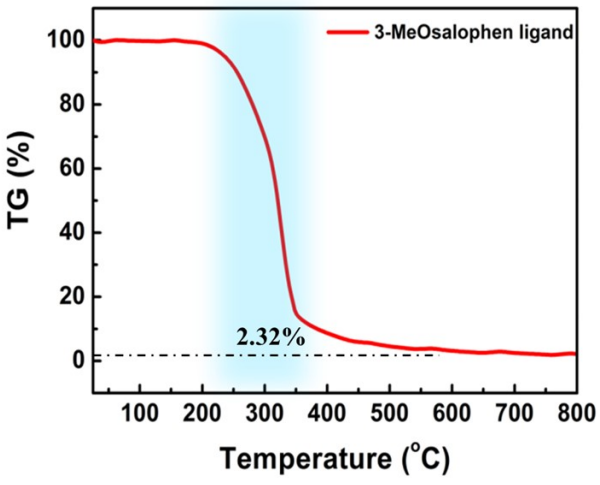

Figure S11 Thermogravimetric curves of 3-MeOsalophen-ligand.

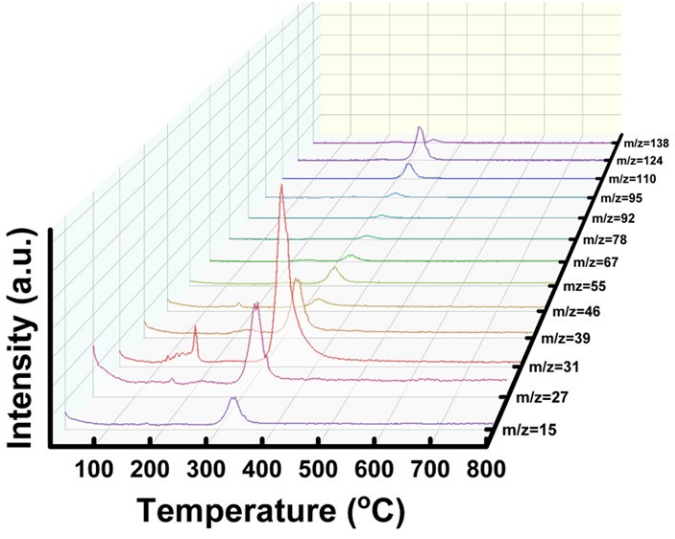

Figure S12 MS curve of 3-MeOsalophen-ligand.

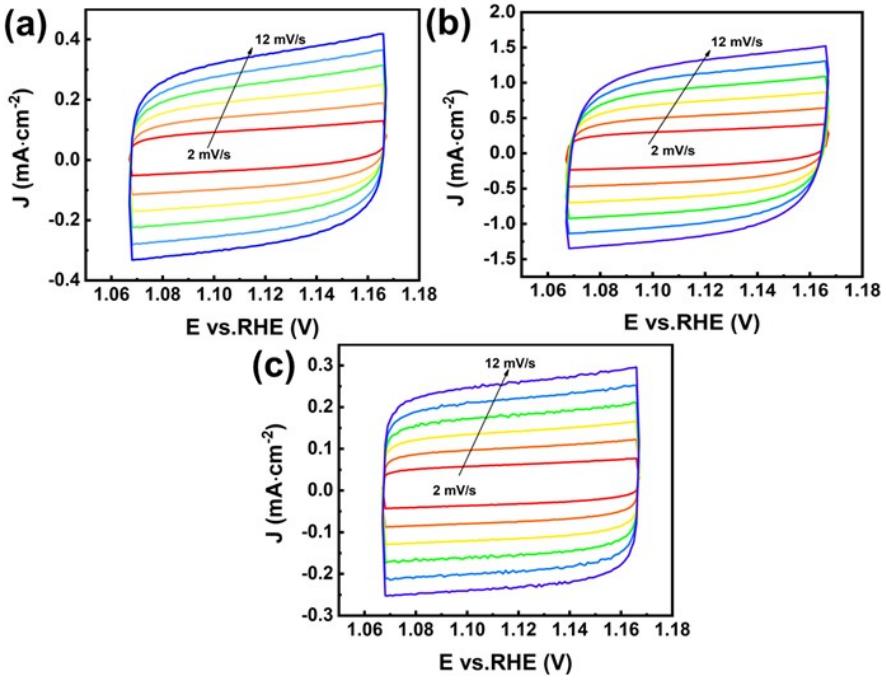

Figure S13 Cyclic voltammograms (CV) measured at scan rates of 2, 4, 6, 8, 10, and 12 mV · s^{-1} on the modified electrode of the pyrolysis product of S-Ni in 1 M KOH aqueous solution in the double-layer capacitor charging region. (a) S-Ni-700, (b) S-Ni-800, (c) S-Ni-900.

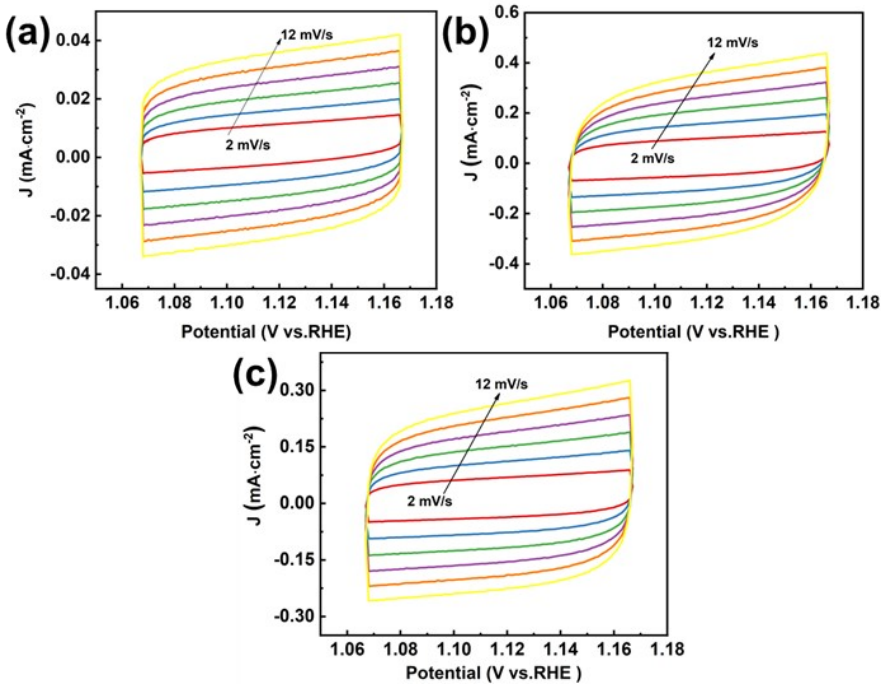

Figure S14 Cyclic voltammograms (CV) measured at scan rates of 2, 4, 6, 8, 10, and 12 mV · s^{-1} on the modified electrode of the pyrolysis product of S-Ni in 1 M KOH + 0.33 M urea aqueous solution in the double-layer capacitor charging region. (a) S-Ni-700, (b) S-Ni-800, (c) S-Ni-900.

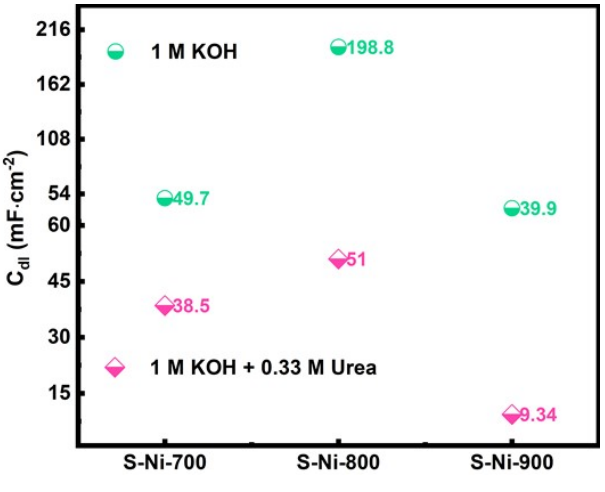

Figure S15 C_{dl} values of S-NI-T(700, 800, 900) catalysts according to CV curve fitting. Green; in 1 M KOH. Pink; in 1 M KOH +0.33 M Urea.

The TOF value was calculated according to the following equation[S15-S17]:

$$TOF = \frac{j * A}{n * F * N} \quad (1)$$

j is obtained at a given overpotential, A is the surface area of the electrode (both front and back sides total about 0.25 cm^2), n is the number of electrons transferred in the electrocatalytic reaction, F is the Faraday constant (96485 C/mol), N is the mole number of metal atoms on the electrode. In this work, since some of these metal sites in the catalyst were electrochemically non-accessible, all the metal ions were assumed to exist on the reactive surface. The turnover frequencies (TOFs) were calculated to assess the intrinsic activity of the S-Ni-700, S-Ni-800 and S-Ni-900 catalysts. The TOF values of S-Ni-700, S-Ni-800 and S-Ni-900 catalysts were 0.11, 0.21 and 0.08 s^{-1} at 1.53 V in 1 M KOH, In 1 M KOH+0.33 M Urea solution, the TOF values are 0.44 s^{-1}, 0.48 s^{-1}, and 0.33 s^{-1}, respectively, indicating that S-Ni-800 exhibits higher intrinsic activity than other catalysts.

$$TON = \frac{The\ number\ of\ electrons\ participating\ in\ the\ reaction}{number\ of\ reactive\ sites} \quad (2)$$

Table S10 Summary of TOF and TON of catalysts in this study.

Sample	1M KOH		1M KOH+0.33M Urea	
	TOF/s^{-1}	**TON/%**	**TOF/s^{-1}**	**TON/%**
S-Ni-700	0.11	23.6	0.44	3.0
S-Ni-800	0.21	90.0	0.48	5.5
S-Ni-900	0.08	18.8	0.33	4.0

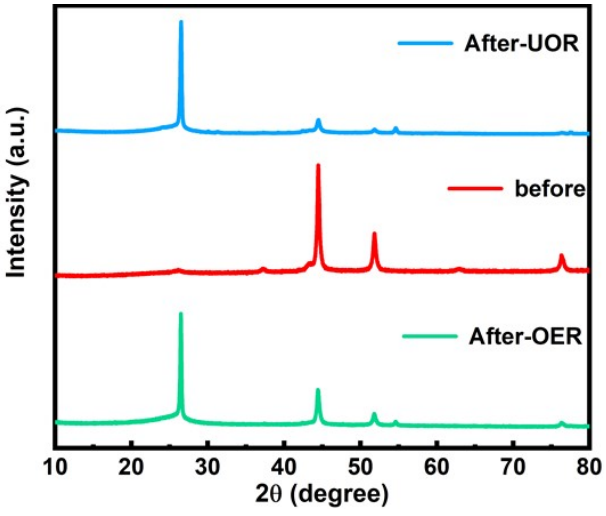

Figure S16 Powder XRD patterns of S-Ni-800 before and after the catalysis were in 1M KOH solution and 1 M KOH+0.33 M Urea.

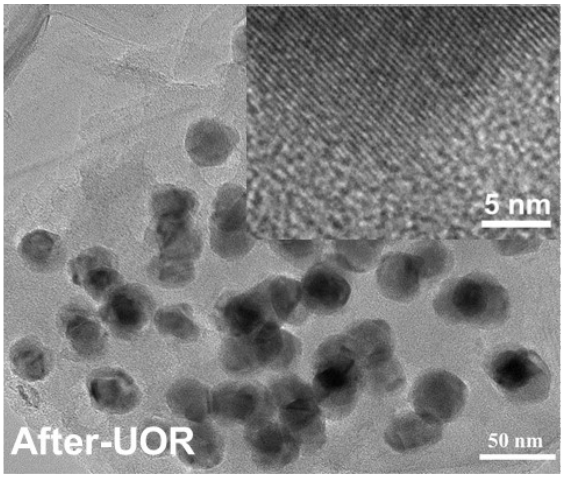

Figure S17 HRTEM image of S-Ni-800 after UOR.

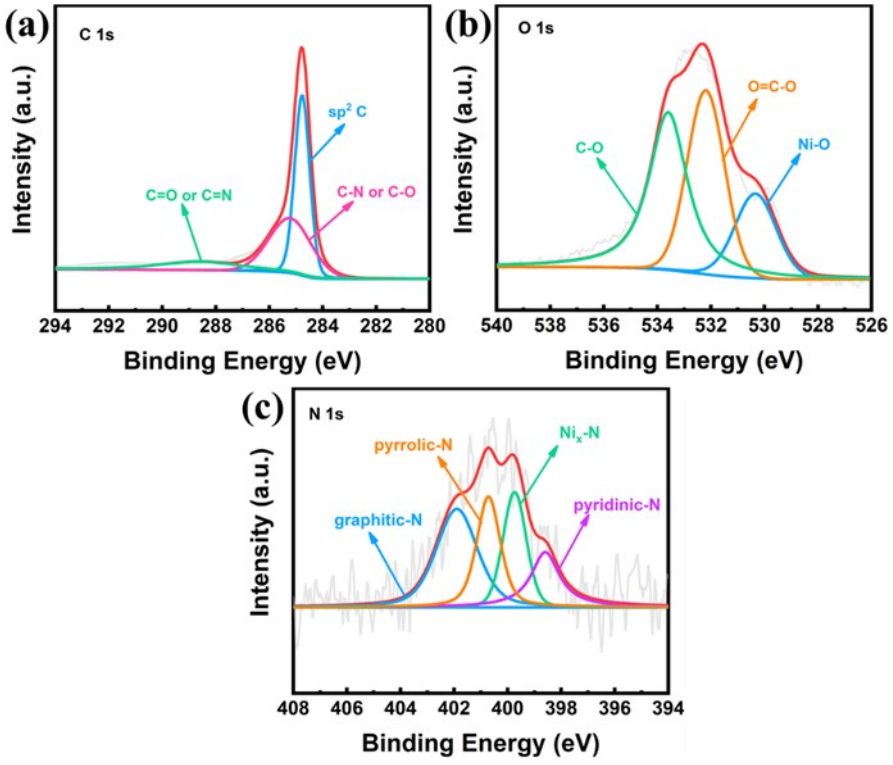

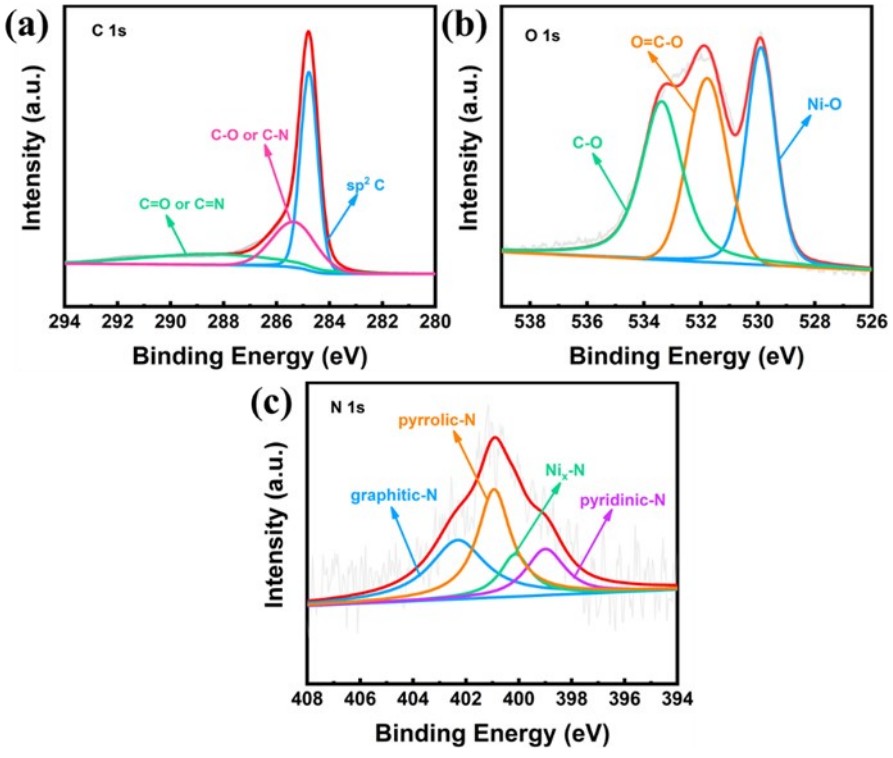

Figure S18 High resolution XPS spectrum of S-Ni-800 after long lime OER. (a) C1s. (b) O1s. (c) N1s.

Figure S19 High resolution XPS spectrum of S-Ni-800 after long lime UOR. (a) C1s. (b) O1s. (c) N1s.

Table S11 EXAFS fitting parameters at the Ni K-edge for After OER/UOR.

Sample	Shell	*CN*	*R*(Å)	σ^2(Å^2)	R_f(%)
Ni foil	Ni-Ni	12	2.48	0.006	0. 5
Beifore	Ni-N/O	0.90	2.06	0.004	1.2
	Ni-Ni	9.87	2.48	0.006	
After OER	Ni-N/O	1.03	2.03	0.006	1.4
	Ni-Ni	9.29	2.48	0.018	
After UOR	Ni-N/O	1.69	2.04	0.007	1.3
	Ni-Ni	8.30	2.48	0.006	

CN: coordination numbers; *R*: bond distance; σ^2: Debye-Waller factors; *R* factor: goodness of fit. *S*02 was set to 0.803, according to the experimental EXAFS fit of Ni foil reference by fixing CN as the known crystallographic value.

Table S12 The estimated volatile products released during the various stages of the thermal decomposition process of the product.

350°C-450 °C	450 °C -900 °C	Selectivity	Total mass released/mg
H_2(m/z = 2)	H_2(m/z = 2)	73.28%	1.5700
C^+ (m/z = 12)	C^+ (m/z = 12)	0.26%	0.0055
CH_4^+ (m/z = 15)		4.98%	0.1070
CO^+ (m/z = 28)		2.54%	0.0545
CH_3O^+ (m/z = 31)		1.34%	0.0287
$C_3H_3^+$ (m/z = 39)		0.61%	0.0131
CO_2^+ (m/z = 44)	CO_2^+ (m/z = 44)	6.79%	0.1459
$C_4H_4^+$ (m/z = 52)		0.38%	0.0081
$C_6H_6^+$ (m/z = 78)		0.25%	0.0054

Most of the ion peaks have a peak between 350 °C and 450 °C. After 600 °C, the intensity begins to increase. This is due to the water vapor reaction produced by the carbon skeleton and steam in the previous pyrolysis process (Eq. ($H_2O+C \rightarrow H+CO$, $C+CO_2 \rightarrow CO$) to produce H_2 and C-H bonds breaking at the higher temperatures.

$$\text{Selectivity} = \frac{Current\ product\ peak\ area}{Total\ product\ peak\ area} \times \%$$

$$Total\ mass\ released = Selectivity \times (raw\ sample\ mass - Remaining\ mass)$$

Among them, the raw sample mass is 2.948 mg, and the remaining product mass is 0.800 mg. The remaining missing parts were undetected as hydrocarbons.

Table S13 Representative high-efficiency OER/UOR catalysts formed by different processing methods from different Ni-based precursors.

Catalyst	**$J_{(mA\ cm^{-2})}$**	**Overpotent.mV (1 M KOH)**	**Tafel slope ($mV \cdot dec^{-1}$)**	**Potent.V 1 M KOH+0.33M Urea**	**Tafel slope ($mV \cdot dec^{-1}$)**	**Ref.**
Ni-MOF/LDH	10	220	36	/	/	S1
Ni-MOF (BTC)	10	346	64	63.15 (1.5 V *vs*. RHE)	/	S2
NP/NiO	10	332	65.6	/	/	S3
FN-2	10	275	56.7	/	/	S4
$NiCo/Fe_3O_4$/MOF-74	10	238	/	/	/	S5
Ni@NiO/N-CNW (250 °C)	10	390	100	/	/	S6
Ni_4N/Cu_3N nanotube	10	/	/	1.34（1.0 M KOH +0.5 M Urea）	55.7	S7
$Ni/NiO@NC_{400}$	10	390	/	1.35 V	19	S8
$Ni_3N/Ni_{0.2}Mo_{0.8}N$	10	257	/	1.328（1.0 M KOH +0.5 M Urea）	17	S9
Ni-Sn sulfide	10	330	/	1.36	32.3	S10
$NP\text{-}Ni_{0.7}Fe_{0.3}$	10	260	29.3	1.55	63.8	S11
NiFeMo	10	230	59.9	1.38	43.3	S12
NiFe-LDH nanosheets	10	225	29	1.35	35	S13
$NiFe(OH)_2$ - SD/NF	10	220	47	1.32	41	S14
S-Ni-700	**10**	**318**	**209**	**1.392**	**110**	**This work**
S-Ni-800	**10**	**268**	**86**	**1.353**	**80.9**	
S-Ni-900	**10**	**343**	**390**	**1.442**	**117**	

References

S1. W. D. Zhang, Q. T. Hu, L. L. Wang, J. Gao and Z. G. Gu, In-situ generated Ni-MOF/LDH heterostructures with abundant phase interfaces for enhanced oxygen evolution reaction, *Appl. Catal. B,* 2021, **286**, 119906.

S2. V. Maruthapandian, S. Kumaraguru, S. Mohan, V. Saraswathy, and S. Muralidharan, An Insight on the Electrocatalytic Mechanistic Study of Pristine Ni MOF (BTC) in Alkaline Medium for Enhanced OER and UOR, *Chemelectrochem*, 2018, **5**, 2795-2807.

S3. P. Bhanja, Y. Kim, B. Paul, Y. V. Kaneti and Y. Yamauchi, Microporous nickel phosphonate derived heteroatom doped nickel oxide and nickel phosphide: Efficient electrocatalysts for oxygen evolution reaction, *Chemical Engineering Journal*, 2021, **405**, 126803.

S4. M. Liu, L. Kong, X. Wang, J. He and X. Bu, Engineering Bimetal Synergistic Electrocatalysts Based on Metal–Organic Frameworks for Efficient Oxygen Evolution, *Small*, 2019, **15**, 1903410.

S5. X. Wang, H. Xiao, A. Li and Z. Li, Constructing NiCo/Fe_3O_4 Heteroparticles within MOF-74 for Efficient Oxygen Evolution Reactions, *J. Am. Chem. Soc*. 2018, **45**, 15336–15341.

S6. A. Xie, J. Zhang, X. Tao, J. Zhang and S. Luo, Nickel-based MOF derived Ni@NiO/N-C nanowires with core-shell structure for oxygen evolution reaction, *Electrochimica Acta*, 2019, **324**, 134814.

S7. J. Li, C. Yao, X. Kong, Z. Li and X. Lei, Boosting hydrogen production by electrooxidation of urea over 3D hierarchical Ni_4N/Cu_3N nanotube arrays, *ACS Sustainable Chem. Eng*. 2019, **15**, 13278–13285.

S8. X. Ji, Y. Zhang, Z. Ma and Y. Qiu, Vacancy-rich Ni/NiO@NC Nanosheets with Schottky Heterointerface for Efficient Urea Oxidation Reaction, *ChemSusChem*, 2020, **13**, 5004-5014.

S9. R. Q. Li, X. Y. Wan, B. L. Chen, R. Y. Cao and Y. C. Zhu, Hierarchical $Ni_3N/Ni_{0.2}Mo_{0.8}N$ heterostructure nanorods arrays as efficient electrocatalysts for overall water and urea electrolysis, *Chem. Eng. J,* 2021, **409**, 1385-8947.

S10. Z. Ji, J. Liu, D. Yang, S. Zhang and X. Lu, Accurate Synergy Effect of Ni-Sn Dual Active Sites Enhances Electrocatalytic Oxidation of Urea for Hydrogen Evolution in Alkaline Medium, *J. Mater. Chem. A*, 2020, **8**, 14680-14689.

S11. Z. Cao, T. Zhou, X. Ma, Y. Shen and Y. Zhao, Hydrogen Production from Urea Sewage on NiFe-based Porous Electrocatalysts, *ACS Sustainable Chem. Eng*. 2020, **29**, 11007–11015.

S12. Z. Lv, Z. Li, X. Tan, Z. Li, R. Wang, M. Wen, X. Liu, G. Wang, G. Xie and L. Jiang, One-step electrodeposited NiFeMo hybrid film for efficient hydrogen production via urea electrolysis and water splitting, *Appl. Surf. Sci.*, 2021, **552**, 149514.

S13. H. Sun, W. Zhang, J. G. Li, Z. Li, X. Ao, K. H. Xue, K. K. Ostrikovc, J. Tang and C. Wang, Rh-engineered ultrathin NiFe-LDH nanosheets enable highly-efficient overall water splitting and urea electrolysis, *Appl. Catal. B,* 2020, **284**, 119740.

S14. P. Babar, A. Lokhande, V. Karade, I. J. Lee and J. H. Kim, Trifunctional layered electrodeposited nickel iron hydroxide electrocatalyst with enhanced performance towards the oxidation of water, urea and hydrazine, *J. Colloid Interface Sci*., 2019, **557**, 10-17.

S15. J. Masud, S. Umapathi, N. Ashokaan, and M. Nath, Iron phosphide nanoparticles as an efficient electrocatalyst for the OER in alkaline solution. Journal of Materials Chemistry A, 2016, **4**, 9750-9754.

S16. Z. Gao, Y. Wang, L. Xu, Q. Tao, X. Wang, Z. Zhou, Y. Lu, J. Yu and Y. Huang, Optimizing local charge distribution of metal nodes in bimetallic metal–organic frameworks for efficient urea oxidation reaction, Chem. Eng. J., 2022, **433**: 133515.

S17. G. Li, S. Li, J. Ge, C. Liu and W. Xing, Uncontinuously covered IrO_2-RuO_2@Ru electrocatalysts for oxygen evolution reaction: How high activity and long-term durability can meet up in the synergistic and hybrid nano-structure? J. Mater. Chem. A, 2017, **5**, 17221-17229.